Solid Freeform Fabrication 2024: Proceedings of the 35th Annual International Solid Freeform Fabrication Symposium – An Additive Manufacturing Conference
Reviewed Paper

EVOLUTION OF POROSITY IN ADDITIVELY MANUFACTURED STEEL 316L DOG BONE SPECIMENS UNDER TENSION: X-RAY COMPUTED TOMOGRAPHY STUDY

Fidel Baez Avila [a], David Moore [b], Borys Drach [a]

[a] Department of Mechanical and Aerospace Engineering, New Mexico State University, Las Cruces NM 88003

[b] Nondestructive Environments and Diagnostics, Sandia National Laboratories, Albuquerque NM 87123

Abstract

An ex-situ study of porosity evolution under tension was performed using X-ray computed tomography (CT). The specimens were manufactured of 316L stainless steel by using laser powder bed fusion (LPBF) to produce dog bone geometry with cross sections of 2.4×2.4 mm^2 and test sections with lengths of 10.4 mm. Five specimens were CT scanned before loading was applied and after each of the three tensile loading steps: (1) 20% strain, (2) maximum force, and (3) failure. CT data were analyzed to compute the volume and maximum linear dimensions of individual pores, as well as to obtain spatial distributions of these quantities within the specimens. Additionally, the fracture surfaces were analyzed using a scanning electron microscope (SEM). Initiation locations of cracks that led to ultimate failure were identified in the initial scans. The results showed that cracks leading to failure grew as a result of the coalescence of small pores in closely spaced clusters in conjunction with small fractures originating on the surface at the same time.

Introduction

Additive manufacturing (AM), commonly known as 3D printing, has revolutionized the way products are designed and manufactured, allowing the creation of complex, custom geometries that would be difficult or impossible to achieve through traditional manufacturing methods. Initially focused on rapid prototyping, AM technologies have evolved to encompass the production of high-quality parts using various materials, including metals.

AM has revolutionized multiple industries by enabling the production of lighter and more complex components in aerospace design, facilitating the creation of customized and optimized parts in automotive fabrication [1], and offering custom implants and prosthetics in medical treatment [1,2]. In the manufacturing sector, it improves the rapid creation of tools and molds [1].

Despite its advantages, metal AM faces significant technical challenges. These challenges include the occurrence of residual stresses that may adversely affect part strength, surface finish issues that require post-processing, and anisotropy that can result in inconsistent mechanical properties depending on the print direction [3]. One of the main challenges is porosity, which refers to the presence of voids in the printed material. Porosity can be caused by various factors such as inappropriate printing parameters or inherent material properties and can negatively influence the quality and mechanical performance of the component. In the context of 3D printed materials,

porosity is defined as the presence of internal voids that have not been filled by the material during the printing process, forming an air bubble or metal powder that did not melt and fuse with the rest of the layer [4,5]. Porosity can significantly reduce the tensile strength, fatigue strength, and impact resistance of printed parts [6]. These voids act as stress concentrators and initiation points for cracks, compromising the structural integrity of the component. To develop rejection criteria for AM parts with pores, it is essential to accurately characterize porosity and how it leads to failure. A detailed understanding of the distribution and size of pores allows for improvements in printing processes and quality of the final parts.

X-Ray Computed Tomography (CT) is a non-destructive (ND) technique that enables detailed characterization of the internal structures of 3D-printed parts. During CT imaging, X-ray projections of the object of interest are captured at various angles by incrementally rotating the specimen. After a full 360-degree rotation, a reconstruction algorithm is employed to create a 3D model [7]. CT offers significant advantages over traditional microscopic analysis – it enables visualization of both surface and internal features of a specimen. Unlike techniques like scanning electron microscopy, which requires special surface coatings to ensure conductivity, CT eliminates this need, providing a more straightforward and versatile analysis. Additionally, because CT is non-destructive, the specimen remains intact throughout the process. [8].

There is limited research on the intermediate stages of the failure process. Most studies focus on the initial state of the specimens and then proceed directly to analyzing the post-failure state. Conversely, this paper instead examines two intermediate states, aiming to identify trends that offer insights into how, when, and where failure is likely to occur. This paper discusses evolution of porosity in LPBF-manufactured stainless steel 316L dog bone specimens under tension. Changes in internal porosity and surface features are tracked by taking CT scans between several loading stages and compared to the undeformed state. Additionally, fractography via SEM is presented.

Materials and methods

Steel Dog Bone Specimens

Five dog-bone shaped specimens were manufactured at Sandia National Laboratories using a direct metal laser sintering (DMLS) machine. The DMLS machine was set up with a laser power of 101 watts and a scanning velocity of 1700 mm per second, using a cross feed of 50 mm. At the point of powder fusion, the beam diameter was 100 mm. A uniform melt pool was promoted by employing a hexagon scan pattern. The layer thickness was set to 30 μm. The powder used had an average diameter of 16.7 μm, with particle size distributions at the 10th percentile (D10) of 9.6 μm and at the 90th percentile (D90) of 25.8 μm. As shown in Figure 1, each dog bone specimen had a nominal test section area of 2.5 by 2.5 mm and a length of 10.43 mm, and featured transitions on both ends to make sure that the stress and strain concentrate in the test section.

Tensile Testing

Tensile loading was applied to the specimens using an Instron 6800 series universal test machine (UTM). Each specimen was subjected to three different loading conditions to observe the evolution of pores and cracks up to ultimate failure and to compare with the undeformed state. In the first loading stage, strain of approximately 20% was applied; this strain was achieved on the UTM by configuring a 2 mm displacement at a rate of 1 mm/min. Note that the specimens were too small for available extensometers, and the only option was to rely on the UTM cross head displacement control. As a result, the 20% value of the applied strain is approximate. The second stage was the maximum force applied to the specimen; the UTM software was configured to automatically stop when the force measured by the machine started to decrease. Finally, the ultimate failure was achieved by pulling the specimens until they broke, and the UTM software was set to stop when the measured force dropped more than 10% from its current value within 100 ms. During the final loading stage, crack propagation resulted in specimen failure. However, the specimen still remained as a single piece, held together by a small bridge, instead of fracturing into two parts. This cohesion facilitated CT scanning and enabled better traceability of pores in the resultant CT data. In accordance with the ASTM standard E8/E8M, a cross head travel speed corresponding to strain rate of 0.15 %/s was used for all tensile testing. For consistency, from this point the loading stages will be referred to as “non-deformed,” “2 mm,” “peak force,” and “break.”

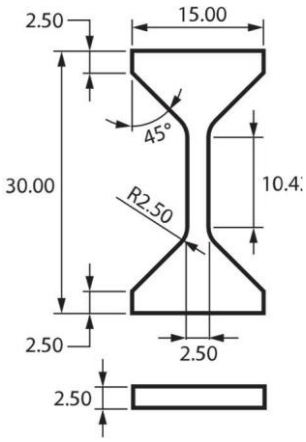

Figure 1:Dimensions of the dog-bone shaped specimens used in this study in mm

CT Imaging

CT scanning was used to visualize internal features and their changes following different loading stages. The specimens were scanned with a Waygate Technologies Phoenix V|tome|xS dual tube CT scanner. The CT machine was configured to produce 14 watts at 120 kV of voltage and 120 µA of current. A total of 1,750 projections were taken, each from a different angle; the exposure time was set to 200 ms, and the detector sensitivity was set to 2. The specimen was placed at 22.94 mm from the X-ray source resulting in a voxel size of 5.5 µm. Three CT scans were taken at different positions along each specimen and stitched together to achieve a full scan of the entire test section. This stitching was performed using the multiscan option. These scan parameters were selected after an iterative process of finding the balance between time required to perform the scanning and quality of the final images. Each specimen was scanned before any loading was applied and following the three previously discussed loading stages. The 3D volume was reconstructed using Phoenix Datos|x 2 software and then converted to an image stack using VG Studio Max. The beam hardening correction tool in the Datos|x 2 software was used.

CT Data Post Processing

Each reconstructed image stack was imported into ORS Dragonfly, where the pores were isolated using threshold segmentation and volume of each individual pore was computed. For each specimen, six different pores were selected at the ends of the test section (three at the top and three

at the bottom) and used for tracking plastic strain after loading. Finally, a MATLAB script was created to plot distribution of the effective load-carrying cross-sectional area (solid portion without porosity) along the test section. As mentioned in the work done by Gong et al., selecting a gray value to fit the whole data set can be difficult and there are variations in each scan even though they share the same setup and parameters [9]. For this reason, the gray values used as a threshold to separate the pores from bulk material were different; however, these values always corresponded to the least frequent value between the two material peaks (air and solid material). Figure 2 shows the reconstructed cross section and the corresponding binarized image.

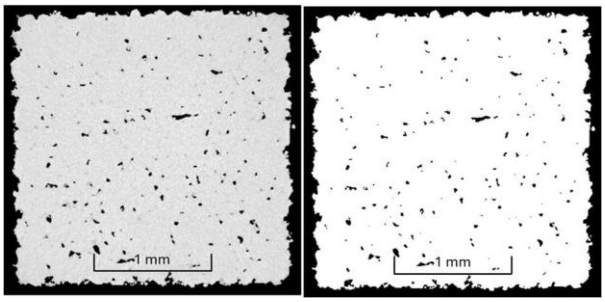

Figure 2: Comparison between a cross section of a dog bone specimen reconstructed from CT imaging and its binarized version.

Scanning Electron Microscopy

The specimens were pulled to separation using the Instron UTM to be broken apart in order to expose fracture surfaces. Once the fracture surface was exposed, the specimens were imaged using a HITACHI ultra-high-resolution Schottky Field Emission Scanning Electron Microscope SU7000 (FE-SEM) at magnification levels of ×800, ×3,000, ×5,000, and ×18,000.

Results and Discussions

CT Parameter Optimization

The initial CT imaging was performed with the following parameters: 25 watts at 125 kV of voltage and 200 μA of current, with a voxel size of 13.07 mm, an exposure time of 200 ms and only one scan was used to completely capture the test section. It can be seen in Figure 3a that the quality of the scan was poor; the pores and edges are not well defined. After moving the specimen closer to the X-ray source, the test section was too big for a single scan. Therefore, the multiscan option was used with three scans per test section. In addition, the number of projections and the exposure time were increased to 1,750 and 1 second, correspondingly. The resulting scan exhibited a significant improvement in quality, see Figure 3b. However, the scan duration for each specimen was 8 hours, which was prohibitively long. The scan parameters presented in the Materials and Methods section were selected following another round of optimization. The final scan time per specimen was 2 hours and 30 minutes and the resulting image is shown in Figure 3c.

Pore and Crack Evolution Observed via CT Imaging

Table 1 presents porosity of each specimen at every stage. Initial pore volume fraction of the specimens is in the range from 0.46% to 0.71% at the non-deformed stage. The porosity increases with every stage, with the only exception of two specimens in which the porosity is lower at the break stage. The decrease at the final stage may be attributed to the way pores are identified in the CT data. For a pore to be identified as such, it must be entirely encircled by the bulk material; any connection to the specimen surface renders it ineligible for classification as porosity.

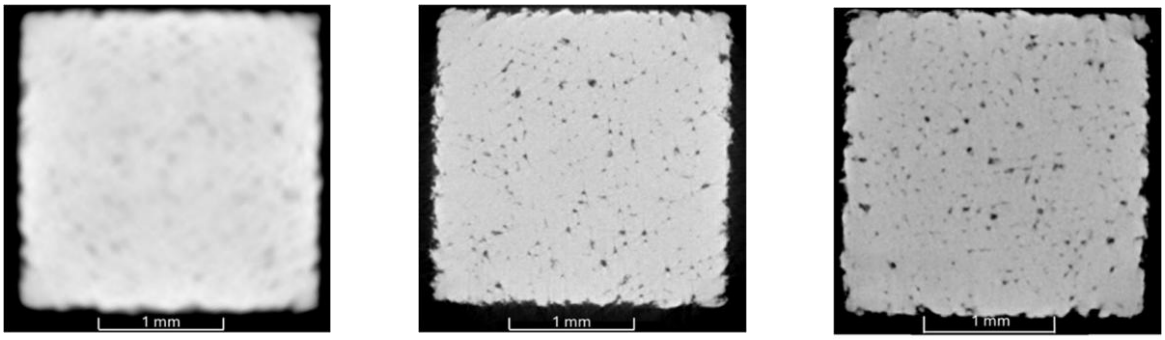

a) b) c)

Figure 3: Comparison of the quality obtained from the CT images showing a) the first scan performed with initial parameters resulting in scan duration of 30 minutes, b) the best quality scan, which took 8 hours, c) the scan with optimized parameters, which took 2 hours and 30 minutes.

Table 1: Porosity fraction (%) of every specimen at every state

Specimen No. / Stage	Non-deformed	2 mm	Peak	Break
12	0.69	1.60	2.19	4.62
16	0.71	1.21	2.24	2.00
33	0.46	0.73	1.47	1.44
44	0.66	0.94	2.22	3.29
51	0.46	1.35	2.29	3.44

Upon closer examination of the CT imaging data and pore size and volume distributions (see Figure 4, Figure 5 and Figure 6), it appears that pores along the entire length of the test section increase in size after each subsequent loading stage. Pore growth depends on the type of the pore – spherical voids (most likely gas porosity) maintain their symmetric shape and between loading stages, while irregularly shaped pores (most likely lack of fusion defects) tend to elongate along the direction of the loading and become slender. In addition to size, the number of pores appears to increase. These pores might be too small in the beginning or be filled with powder particles so they cannot be resolved in the CT imaging until a small deformation is applied to the specimens and they increase in size.

In the specimens studied, two failure propagation behaviors have been observed (see Figure 5 and Figure 6). The first one consists of a valley growing from the surface to the inside of the specimen. These small cracks start developing everywhere along the test section. The second behavior consists of a cluster of pores coalescing into larger pores. These larger pores reduce cross-sectional area and create a high-stress concentration zone. This high-stress zone enhances the growth of internal pores and surface cracks until they connect and merge. In some specimens there were two or more clusters of pores that coalesced to form larger pores; however, only one cluster

reached the surface crack and caused ultimate failure in each case. This finding complements what Carlton et al. proposed, where not only the internal pores are relevant for the final fracture but also the presence of an external crack [10].This situation can be seen in Figure 5 (c) and (d), where there are three main clusters of pores, but only the cluster in the middle is close to a surface crack, and it resulted in the ultimate failure.

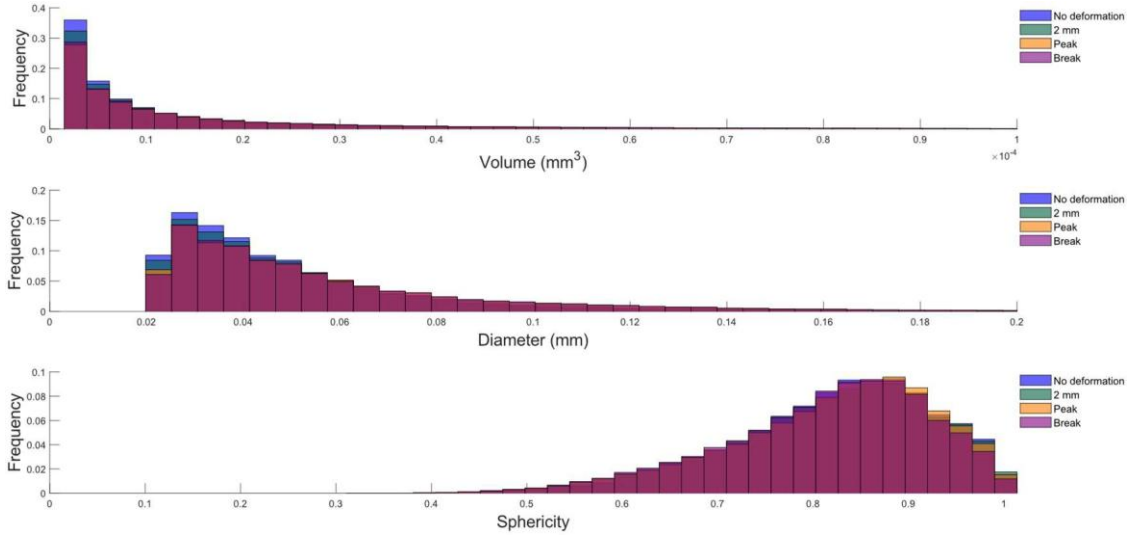

Figure 4: Pore volume, diameter, and sphericity distributions for specimen 16.

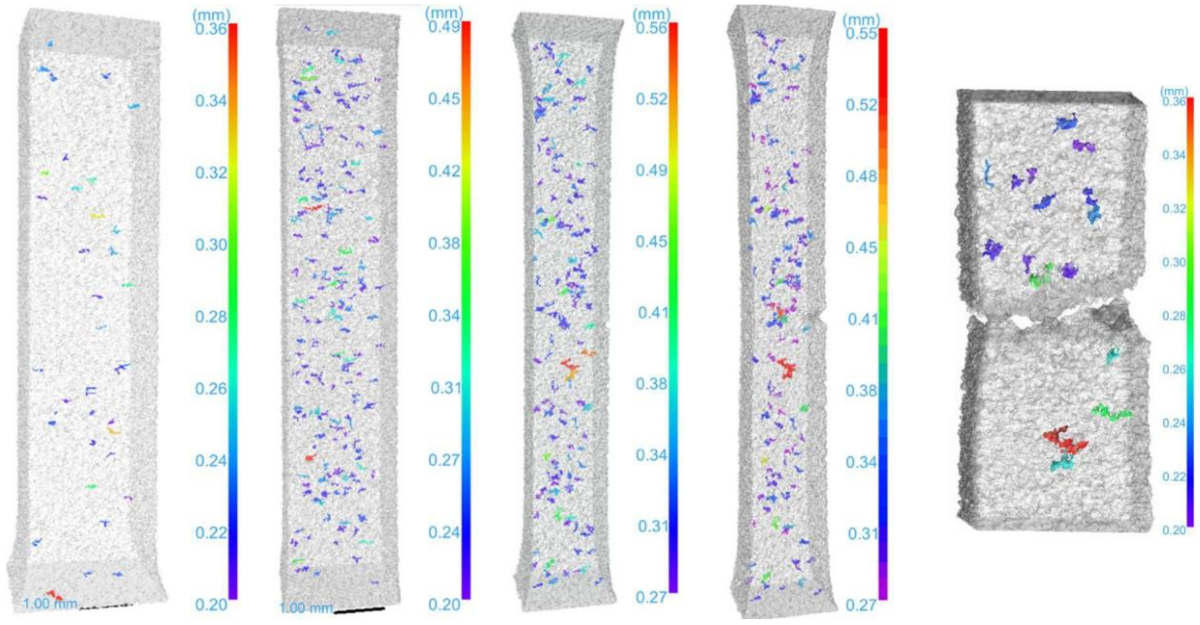

(a) (b) (c) (d) (e)

Figure 5: 3D visualization of the pore distribution in specimen 16 at different stages: (a) non-deformed, (b) 2 mm, (c) peak force, (d) break, (e) specimen separation. Pores smaller than 0.2 mm are hidden in all images. The scale bar changes for every stage.

In Figure 5 (e) the middle cluster finally merged with the crack that initiated at the surface and resulted in specimen separating into two halves. Figure 6 shows that the crack that led to ultimate failure was originally a feature of the surface roughness. Note, that the crack partially closes due to elastic recovery following removal from the UTM grips. As a result, the full extent of the crack may not be visible on CT imaging.

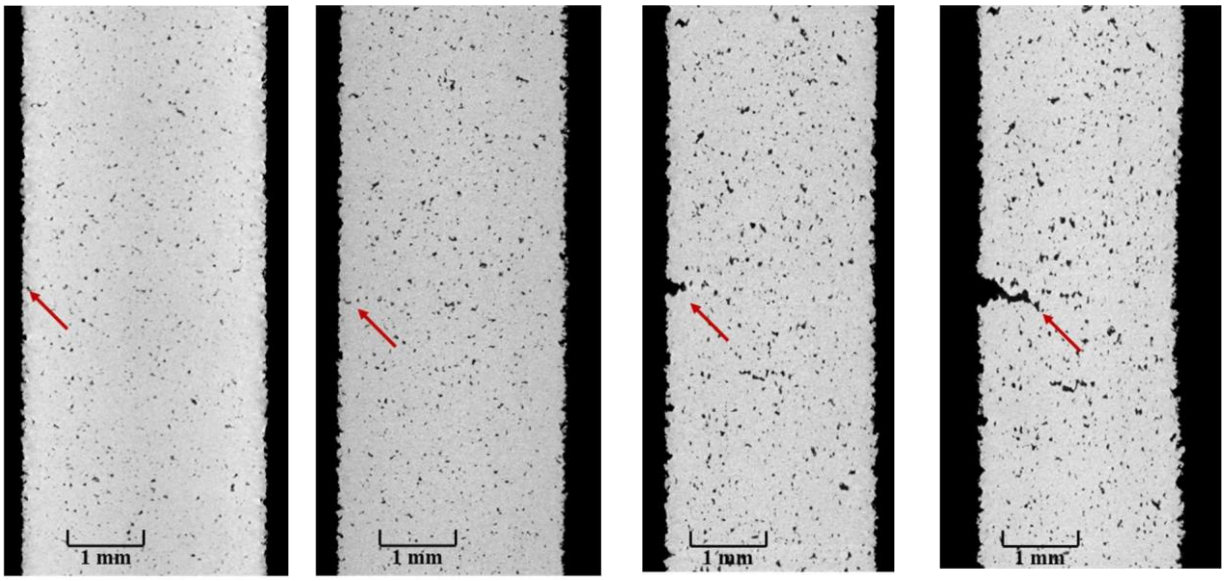

(a) (b) (c) (d)

Figure 6: Reconstructed CT imaging slices of the same cross section throughout the four stages, showing pore and crack growth: (a) non-deformed, (b) 2 mm, (c) peak, and (d) break.

Strain Calculations

Table 2 presents plastic strain computed by tracking distances between pores at the ends of the test section in the CT data. As expected, the strain increases as the specimens are subjected to tension. Collected CT data reflects solely the plastic strain effect because the data was obtained after the specimens were removed from the UTM grips. Alternative methods, such as extensometer or digital image correlation (DIC), would have provided an optimal approach for obtaining the overall strain. These methods would enable the quantification of plastic strain similarly to the method described in this paper, while also providing access to the elastic portion through DIC data. Unfortunately, due to the size of the specimens, these measurement methods were not available.

According to Jost et al., the maximum strain exhibited by AM stainless steel 316L must be around 60% [11]. In Table 2 it is apparent that four out of five specimens demonstrate a maximum strain close to 60%. Discrepancies among the specimens can be attributed to the inherent variability of the AM process, which yields non-identical specimens.

Table 2: Computed plastic strain (%) for every specimen at every state, along with the force required to break each specimen.

Specimen No. / Stage	2 mm	Peak	Break	Maximum force (kN)
12	12.8	42.4	48.6	3.17
16	10.9	61.0	67.6	3.05
33	11.2	37.8	58.1	3.09
44	13.2	42.1	64.1	3.05
51	11.7	39.7	56.1	2.99

Effective area computations

A MATLAB script was developed to binarize each cross-section slice along the test section and calculate the "effective area" or area of the bulk material without the pores. The area values were normalized by the nominal cross-sectional area (see Figure 1 for specimen dimensions). Figure 7 shows variations in the effective area along test section for each loading stage in the five specimens (running average of 20 slices is presented for visualization purposes). The vertical axis corresponds to the height at which the effective area is located. A relatively uniform reduction in the test section's area is apparent after the first loading stage which is expected due to the Poisson's effect; however, localization in area reduction can already be observed after the "peak" loading stage. This localization coincides with necking location at the break stage showing how much the cross-sectional area decreases at the necking location at an early stage. Finally, the location of the crack can be identified by the regions with the lowest effective cross section area at the break stage. Closer examination of the effective area distribution in the undeformed state reveals significant fluctuations in the effective area, along with localized regions of several neighboring slices having smaller areas.

In particular, in specimens 12 and 51 clusters of cross sections with relatively low normalized areas are particularly pronounced in the effective area plots before deformation, and they coincide with eventual fracture locations; however, this trend is observed across all specimens; see locations identified by red arrows in Figure 7 ND. Note how the effective area of these regions is smaller than the average cross-section area of the whole test section (dashed line) for a relatively long portion of the specimens compared to the fluctuations below and above average area in other regions of the specimens. This behavior suggests the potential to predict fracture-prone regions using CT data collected on undeformed specimens. This approach could potentially lead to mitigation of risks associated with the final product and reduce costs related to maintenance, repairs, or replacements. Additionally, the approach enables informed design modifications to accommodate effective area variations, optimizing load distribution and cross-section design. However, a larger study would be required to come up with a criterion for identifying critical location based on effective area plots.

Fractography Results

The consistent patterns observed in the FE-SEM microscopy images (Figure 8) across various specimens indicate a distinct behavior of fractures in the proximity of pores. Initially, the fractures exhibit a brittle nature, evident from the presence of cleavage patterns surrounding the pores; see Figure 8e where the arrow points towards a pore with cleavage patterns. Subsequently, the fracture behavior undergoes a transition to a mixed mode characterized by the coexistence of brittle and ductile behaviors, as denoted by the appearance of dimples on the cleavage patterns (see Figure 8c) pointed by the arrow on Figure 8d). Fully ductile behavior is manifested, featuring a notable abundance of dimples in the regions connecting areas between pores; see Figure 8a and b. This behavior verifies that the presence of pores diminishes the mechanical properties of the specimens, not only by reducing the effective area but also by precipitating low-energy fractures. Finally, in Figure 8e) a spherical feature can be observed; this feature is a powder particle that did not melt during the AM process, resulting in porosity due to lack of fusion. Assuming the initial pore had a size similar to the particle, it can be seen how much pores grow and get deformed after loading.

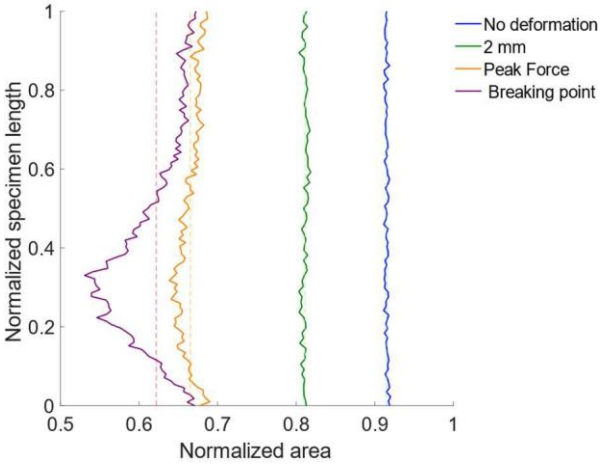

(a)

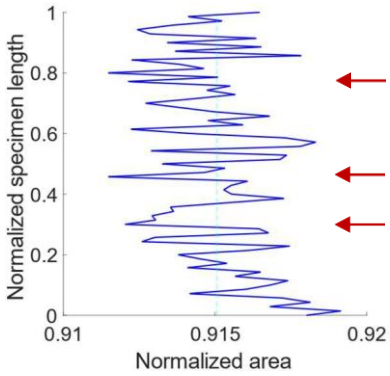

(a - ND)

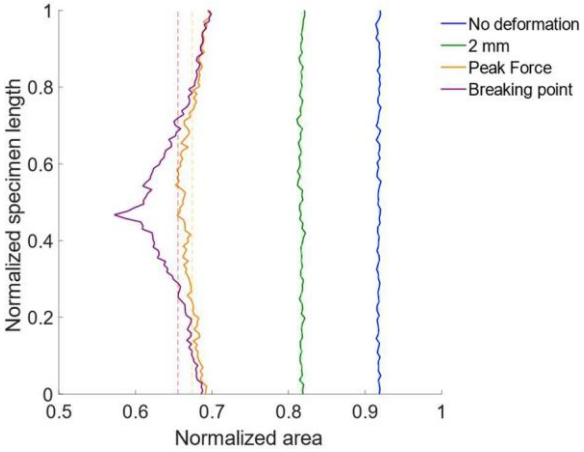

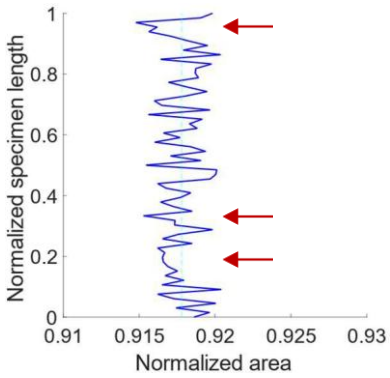

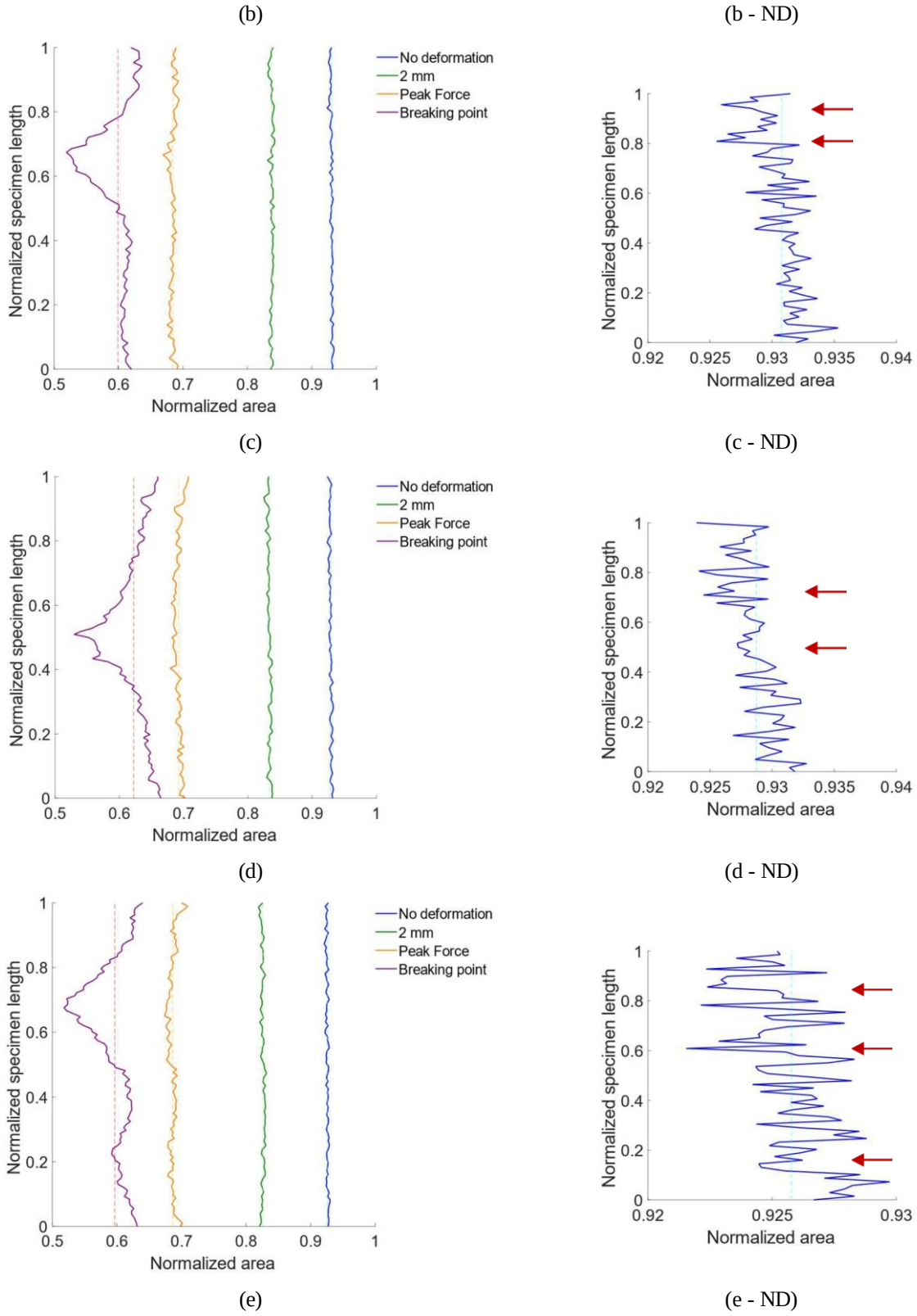

Figure 7: Effective area distributions captured at different loading stages and a detailed view of the distribution at the "non-deformed" stage for specimens (a) 12, (b) 16, (c) 33, (d) 44, (e) 51. Red arrows point towards the locations with smaller effective areas, which may lead to localized stress concentration and contribute to pore and

crack growth. Note, running average of 20 slices is presented for visualization purposes – the entire test section of each specimen is represented by approximately 1000 slices before averaging.

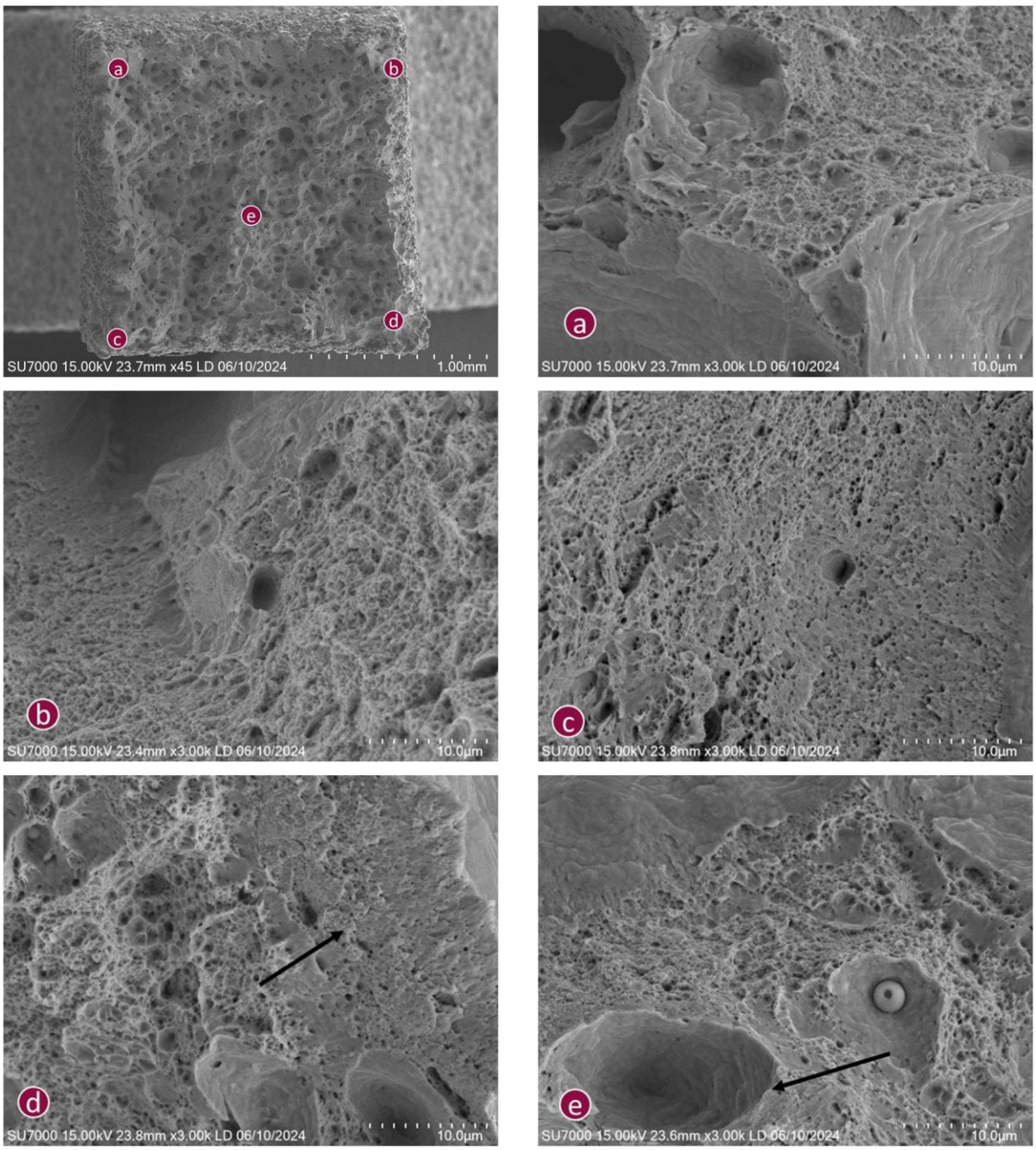

Figure 8: FE-SEM fracture surface images obtained for specimen 16.

Figure 9 illustrates the fracture surface of specimen 16 imaged by two techniques, CT and FE-SEM. CT can be used to locate the initiation site of the crack and pore cluster that facilitated ultimate failure. This localization is evident from examination of the sequential CT scans following

the considered loading stages. On the other hand, FE-SEM results in a more detailed image of the fracture surface. Contrary to what Dressler et al. saw on their specimens, here we cannot easily identify where the crack was initiated since there is no clear slip plane or any other indicator [12]. Using CT, the initial crack was tracked, and it is pointed in Figure 9 at the bottom right corner in this specimen.

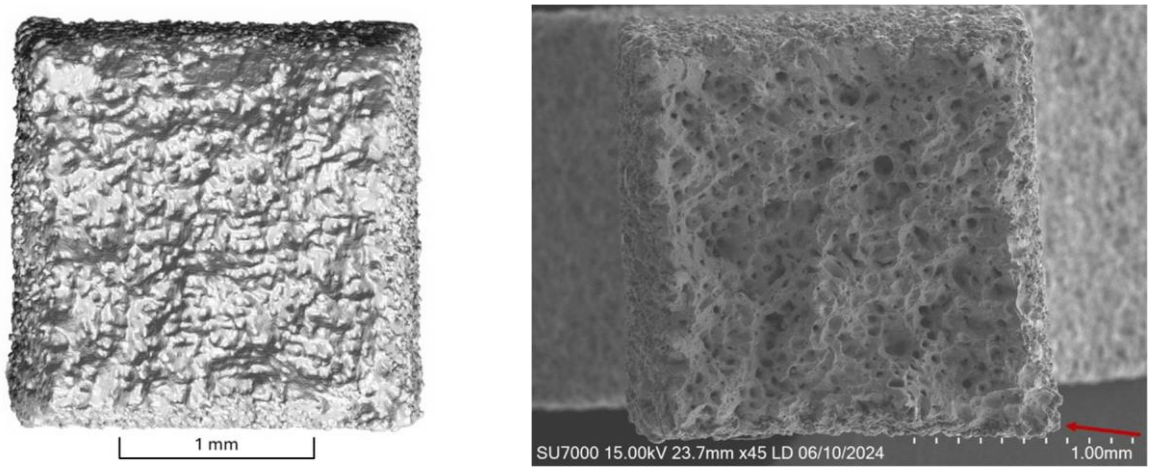

(a) (b)

Figure 9: Fracture plane of specimen 16 imaged via: (a) CT, (b) FE-SEM.

Conclusions

A combination of destructive and non-destructive techniques was used to investigate pore growth and crack development in AM steel 316L specimens under tension. In the five specimens analyzed in this paper small cracks formed on the surface of the test section and progressed toward the interior of the specimen, while gas and lack of fusion pores grew and coalesced internally. As a result of crack and pore cluster growth, eventually the two defects coalesced, leading to ultimate failure.

Computed tomography of as-built specimens can be used for imaging non-uniform distributions of defects resulting from additive manufacturing process variability. In this study pores as small as 20 μm were quantified. There appears to be potential for identification of future failure initiation locations using CT imaging of porosity in the non-deformed state processed to obtain an effective-area distribution plot; with the ultimate failure happening at the locations with lower effective areas as seen in the non-deformed state. Elastic recovery results in partial closure of propagated cracks and makes resolving the full extent of the cracks difficult with CT imaging. The use of a special fixture of holder to prevent cracks from closing may be necessary to get more details about crack propagation at every loading stage. Future work could focus on using two-point correlation for a more precise identification of pore clusters and surface defects that may lead to failure.

Acknowledgements

This research is based upon work supported by the National Aeronautics and Space Administration under the NASA Cooperative Agreement No. NM-80NSSC20M0215, the Army Research Office under the grant No. W911NF2110138, and the National Science Foundation under the grant No. CMMI-2215982.

Sandia National Laboratories is a multi-mission laboratory managed and operated by National Technology & Engineering Solutions of Sandia, LLC (NTESS), a wholly owned subsidiary of Honeywell International Inc., for the U.S. Department of Energy's National Nuclear Security Administration (DOE/NNSA) under contract DENA0003525. This written work is authored by an employee of NTESS. The employee, not NTESS, owns the right, title and interest in and to the written work and is responsible for its contents. Any subjective views or opinions that might be expressed in the written work do not necessarily represent the views of the U.S. Government.

References

[1] Ngo, T., Kashani, A., Imbalzano, G., Nguyen, K., and Hui, D., "Additive Manufacturing (3D Printing): A Review of Materials, Methods, Applications and Challenges," Composites Part B: Engineering, **143**(June 2018), pp. 172–196.

[2] Velasquez Garcia, L. F., and Kornbluth, Y., "Biomedical Applications of Metal 3D Printing," Annu Rev Biomed Eng, (July 2021), p. 307 338.

[3] Kok, Y., Wang, P., Nai, M. L. S., Loh, N. H., Liu, E., and Tor, S. B., "Anisotropy and Heterogeneity of Microstructure and Mechanical Properties in Metal Additive Manufacturing: A Critical Review," Materials & Design, **139**(2018), pp. 565–586.

[4] Laursen, C., De Jong, S., Dickens, S., Exil, A., Susan, D., and Carroll, J., "Relationship between Ductility and the Porosity of Additively Manufactured AlSi10Mg," Materials Science & Engineering A, **795**(23 September 2020).

[5] Huang, Y., Leu, M., Mazumder, J., and Donmez, A., 2015, "Additive Manufacturing: Current State, Future Potential, Gaps and Needs, and Recommendations," Journal of Manufacturing Science and Engineering, **137**(1), pp. 137–147.

[6] Al-Maharma, A., Patil, S., and Markert, B., "Effects of Porosity on the Mechanical Properties of Additively Manufactured Components: A Critical Review," Material Reseasrch Express, **7**(2020).

[7] Thompson, A., Maskery, I., and Leach, R., 2016, "X-Ray Computed Tomography for Additive Manufacturing: A Review," Measurement Science and Technology, **27**(072001).

[8] Shrestha, S., Starr, T., and Chou, K., "Porosity Analysis in Metal Additive Manufacturing by Micro-CT," ASME 2018 International Mechanical Engineering Congress and Exposition, (January 15, 2019).

[9] Gong, H., Nadimpalli, V., Rafi, K., Starr, T., and Stucker, B., "Micro-CT Evaluation of Defects in Ti-6Al-4V Parts Fabricated by Metal Additive Manufacturing," Technologies, **7**(2019).

[10] Carlton, H., Haboud, A., Gallegos, G., Parkinson, D., and MacDowell, A., "Damage Evolution and Failure Mechanisms in Additively Manufactured Stainless Steel," Materials Science & Engineering A, **651**(2016), pp. 406–414.
[11] Jost, E., Miers, J., Robinson, A., Moore, D., and Saldana, C., 2019, "EFFECTS OF SPATIAL ENERGY DISTRIBUTION ON DEFECTS AND FRACTURE OF LPBF 316L STAINLESS STEEL," Solid Freeform Fabrication 2019: Proceedings of the 30th Annual International Solid Freeform Fabrication Symposium – An Additive Manufacturing Conference.
[12] Dressler, A., Jost, E., Miers, J., Moore, D., Seepersad, C., and Boyce, B., "Heterogeneities Dominate Mechanical Performance of Additively Manufactured Metal Lattice Struts," Additive Manufacturing, **28**(2019), pp. 692–703.